ADVANCED OPTICAL MATERIALS
www.advopticalmat.de

Optimization of the Bulk Refractive Index Sensitivity of Silver NanoPrisms

Géza Szántó, Pia Pritzke, Jonas Jakobus Kluitmann, Johann Michael Köhler, Andrea Csáki, Wolfgang Fritzsche, István Csarnovics, and Attila Bonyár*

The sensitivity and optical properties of silver nanoprisms (triangular plates with round-truncated corners) are investigated in this paper. Results of boundary element method simulations are compared with experimental results and literature data. Based on electron microscopy images of the synthesized nanoprisms, a single-particle model is set up for simulations with three running parameters: edge length, thickness, and roundness (defined as the radius of the circumscribed circle divided by the edge length). These geometric parameters can be optimized during chemical synthesis to create sensors with improved sensitivity. The effect of biomolecular layers is also investigated. As a novel approach to improve the agreement between the simulated and experimentally measured extinction spectra, the single-particle model is extended to consider the variation of the prisms' parameters in the form of distributions. The resulting extinction cross-section spectra correspond well with the experimental data. The calculated bulk refractive index sensitivity is 670 nm/RIU (RIU stands for refractive index unit) for the single particle model (length = 150 nm, thickness = 10 nm, and roundness = 0.1), while (690 ± 5) nm/RIU for the extended model. The presented model and obtained relations between sensitivity and geometry can be effectively used to design and optimize the fabrication technologies for silver nanoprism-based sensing applications.

1. Introduction

Plasmonic nanostructures, especially noble metal nanoparticles, form the basis of innovative sensors as optical signal converters.[1] The use of plasmonic nanoparticles could enable the future realization of novel, label-free, and cost-effective sensors for analytical diagnostics.[2] The fundamental physical effect utilized for sensing in these nanoscale structures is the occurrence of the so-called localized surface plasmon resonance (LSPR), a collective oscillation of free conduction electrons upon the interaction of photons of the incident light with the electrons. The result is strong absorption and scattering, as well as local field enhancement around the particles, which depends on the particles' material, shape, and size.[3,4] These factors can be targeted with colloidal chemical synthesis. It is important to note that the local dielectric environment of metallic nanoparticles also plays a crucial role in the occurrence of LSPR. Therefore, nanoparticles can be utilized to monitor the refractive index of their environment, which is the ultimate goal for sensors based on LSPR.

Nanospheres of desired dimensions and materials can be synthesized by the reduction of metal salts. Colloidal gold is one of the most common particle types. It offers high chemical stability and can be easily bioconjugated or otherwise functionalized for various applications.[5] However, the spectral range of such nanoparticles is quite narrow (≈520–580 nm), which could limit the

G. Szántó, I. Csarnovics
Department of Experimental Physics
Institute of Physics
Faculty of Science and Technology
University of Debrecen
Bem tér 18/a, Debrecen 4026, Hungary
E-mail: szanto.geza@science.unideb.hu

The ORCID identification number(s) for the author(s) of this article can be found under https://doi.org/10.1002/adom.202302967

DOI: 10.1002/adom.202302967

P. Pritzke, A. Csáki, W. Fritzsche
Leibniz Institute of Photonic Technology
Member of Leibniz Research Alliance Health Technologies
Albert-Einstein-Strasse 9, 07745 Jena, Germany

J. J. Kluitmann, J. M. Köhler
Institute for Chemistry and Biotechnology
Department of Physical Chemistry and Microreaction Technology
Technical University Ilmenau
Ehrenbergstraße 29, 98693 Ilmenau, Germany

A. Bonyár
Department of Electronics Technology
Faculty of Electrical Engineering and Informatics
Budapest University of Technology and Economics
Egry József utca 18, Budapest 1111, Hungary

A. Bonyár
Wigner Research Centre for Physics
Konkoly-Thege Miklós út 29-33, Budapest 1121, Hungary

applicability. Moreover, as a quantitative indicator for the sensitivity, the plasmon resonance shift per refractive index unit is not particularly high for gold spheres. Much higher sensitivities can be achieved with silver as a material.[6] For silver particles, both the absorption and the scattering cross-sections are at least one order of magnitude higher than with gold of the same geometry.[7,8] In addition to the material, the geometry of the nanoparticles plays an important role in sensing.[9,4] The appearance of corners and edges creates local hot-spots, and additional electron oscillations are enabled by changing the aspect ratios. For example, transverse and longitudinal oscillations occur in nanorods[10] and in-plane and out-of-plane resonances in prisms.[11] Meanwhile, a wide variety of particle shapes can be chemically prepared and are being tested for various sensory applications. In order to propose more sensitive particle shapes, theoretical studies of the effects of particle geometry on the expected sensitivities represent an important field of research. In addition to rods[12,13] and prisms,[14,15] nanostars,[16] cubes,[17–19] bipyramids, dumbbells, dog bones,[20] nanocages,[21] and a variety of their transition forms[22] are chemically accessible.

If plasmonic nanoparticles are to be used in optical biosensing, nanoparticles with the highest sensitivities should be produced wherever possible.[23,4] These play a role in several different types of sensing: in refractive index sensing, more sensitive nanostructures achieve a higher shift in wavelengths,[24,25] in surface-enhanced Raman spectroscopy (SERS[26]) and in enhanced fluorescence,[27] a higher gain factor. In the presented paper this optimization is in the focus. Therefore, the sensitivity can be predicted by the potential possibility of influencing the most important factors, such as material, dimension, and shape, during the chemical synthesis. Especially the geometric factors are at the center of attention. Simulations can be performed for nanoparticles, especially silver nanoprisms, to optimize the necessary geometry for optimal sensing.

Among the large number of available options, the boundary element method (BEM) was selected.[28–30] Other numerical methods used for plasmonics (a non-exhaustive list): finite-difference time-domain (FDTD),[31] discrete dipole approximation (DDA), finite element method (FEM). BEM outperforms all items on this list in terms of simulation speed. In contrast to other techniques, the boundary element method requires only the discretization of the particle's surface rather than its entire volume. For the same reason, the method is characterized by low computational and storage demand. The complex parameterization of the boundary elements could represent a disadvantage, but only for complicated particle shapes.[29,30] BEM approaches are suitable for near- and far-field simulations. The implementation used in the toolbox differs from the usual field-based approach, and utilizes the scalar and vector potentials to solve the full Maxwell's equations.[32]

In this paper, a theoretical study of the sensing capabilities of silver nanoprisms is presented. The effect of edge length, thickness, and roundness of the silver prisms on their sensitivity is investigated and compared with experimental data from the literature.

The purpose of this study is twofold: On the one hand, it investigates which models and assumptions can be used to model the experimental spectrum of nanoprisms. On the other hand, it investigates tendencies from the results of the simulations, e.g., the relationship between the main geometric parameters and extinction peak position and sensitivity, which characteristics may help in the optimization of fabrication technologies, considering sensing applications.

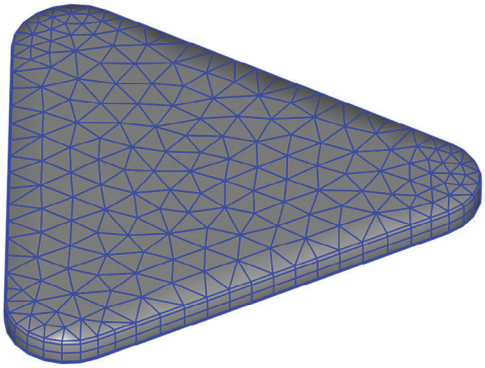

Figure 1. The BEM model with the applied mesh for the default particle in a tilted view. (l = 150 nm, thickness: $t = 10$ nm, roundness: $\gamma = 0.1$).

2. Results and Discussion

2.1. Nanoprism Simulations Based on Experimental Data

The optical properties of the nanoparticles were examined as a function of three parameters: edge length (l), thickness (t), and roundness ($\gamma = r/l$, where r is the initial radius of the rounded corners). The edge length is defined as the distance between the vertices of the rounded corners.

The steps of creating a particle are the following: 1) creating a regular (non-truncated) 2D triangle with a side length of l; 2) rounding the corners with a radius of r (i.e., the edge length is shortened), which yields $\gamma = r/l$; 3) enlarging the triangle to regain the original edge length of l (the final radius is larger than r); 4) extruding a 3D particle with a thickness of t.

Based on scanning electron micrographs of the experimentally synthesized nanoparticles (with parameters presented in Section 2.2), the median values of the geometric parameters for the prism-shaped particles in the sample (referred to as "default particle" from now on) are the following: edge length: $l = 150$ nm, thickness: $t = 10$ nm, roundness: $\gamma = 0.1$ (**Figure 1**). Based on the SEM images, which showed particles very similar to each other, only a range slightly different from the parameters of the default particle was examined.

To map the excitable modes, the averaged spectrum obtained by many random rotations of the default particle was first examined, as presented in **Figure 2**. In all cases, the particles were lying on the XY plane, and a linearly polarized propagating wave in the Z (normal) dimension was used to illuminate them. Figure 2 compares the averaged extinction spectrum yielded by random orientations with the spectrum of a particle illuminated with a polarization vector pointing toward one of the tips of the triangle. The fact that the two spectra coincide means that modes excited beyond the primary mode on the three tips contribute insignificantly to the averaged spectrum. The bulk refractive index sensitivity obtained for the primary mode is the same as for the rotation averaged case: 670 nm/RIU. Since there is only a tenth of

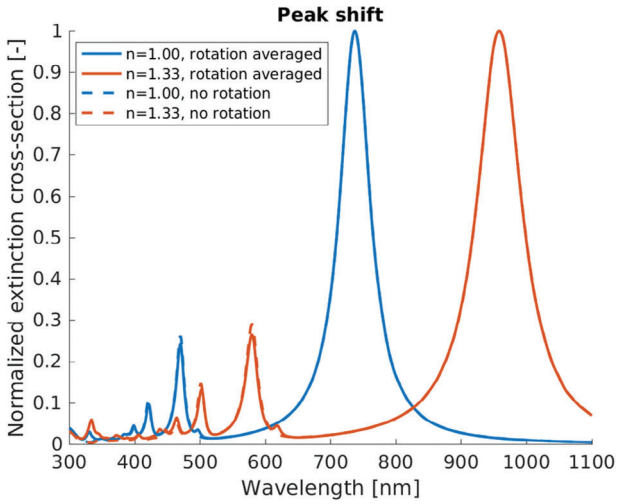

Figure 2. Shift of the resonance peak due to refractive index change from 1.00 (blue) to 1.33 (orange). Note that the spectra for rotation averaged (solid line) and not rotated ones (dashed line) overlap almost completely in both cases.

a nm difference between the results, the effect of particle rotation can be neglected for further calculations concerning sensitivity.

By comparing the simulation result with the experimental spectra, only a moderate qualitative agreement is observed (**Figure 3**). The shapes of the spectra are similar, but the experimental spectra have much broader peaks. There is a 42 nm difference between the position of the main peaks: for $n = 1.33$, the experimental peak position is at 1000 nm, while the simulation resulted in 958 nm.

This difference may be partly due to the capping agents on the real silver nanoparticles. However, the most significant effect is likely due to the size and shape distribution of the particles. Both of the possible options will be analyzed in detail below. The synthesized particles and their distribution are illustrated in the SEM image of **Figure 4**. A histogram for these particles' height

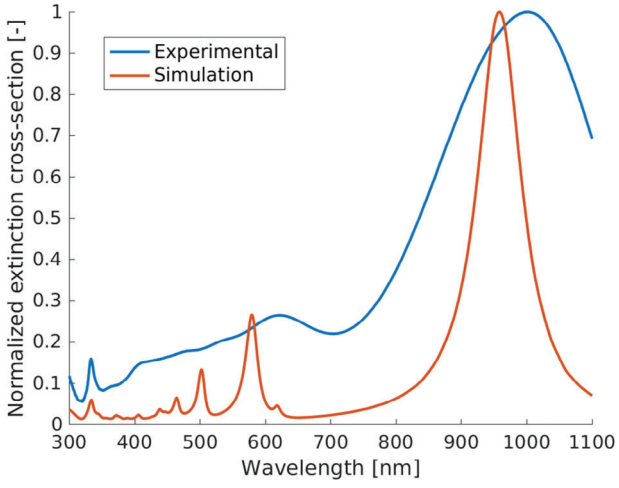

Figure 3. Comparison of the experimental extinction spectrum with a theoretical one, obtained from the synthesized particles, single-particle model at $n = 1.33$ condition (edge length $l = 150$ nm, thickness: $t = 10$ nm, roundness: $\gamma = 0.1$).

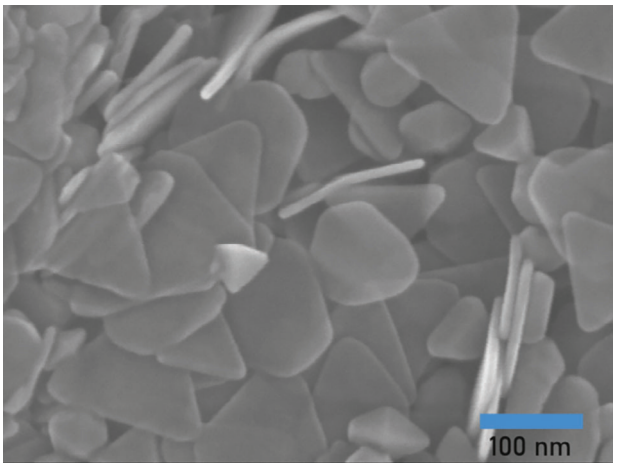

Figure 4. SEM-image of the chemically synthesized nanoprisms with a dimension of $l = 152 \pm 19$ nm, $t = 11 \pm 1.6$ nm.

and edge length can be found in the Supporting Information (Figure S2, Supporting Information).

The most important observable differences between the single-particle model and the experimentally synthesized particles are:

1) The size distribution of the particles most likely follows a distribution that is not considered in the simple model discussed so far. The size of the particles may follow a lognormal distribution,[33,34] which can be well approximated by a Gaussian distribution in the case of a small standard deviation.
2) The synthesis of shape-anisotropic nanoparticles is far more complex than that of spherical nanoparticles, which is why other geometries are also represented in the final product besides the desired prisms. (Their effect is also neglected in the following sections.)
3) Slightly larger particles than average (which have an extinction peak at a longer wavelength) are approximately in comparable numbers as slightly smaller ones (peak at shorter wavelengths). However, the larger particles dominate the spectrum because they have more intense extinction cross-sections. Overall, the peak of the averaged spectrum of particles following a Gaussian distribution is located at a higher wavelength than the peak of the spectrum of the average-sized particle.

It can be assumed that the size distribution may be responsible for almost the entire deviation between the experimental spectrum and the simulation results. Before delving into the details of size distribution (Section 3.5), it is important to understand the impact of geometrical parameters on the results of the single-particle model.

2.2. Refractive Index Sensitivity

2.2.1. Extinction Spectrum and Sensitivity as a Function of (l, t, γ) Parameters

This section examines the effect of l, t, and γ on the bulk refractive index sensitivity of a single particle. Although these parameters

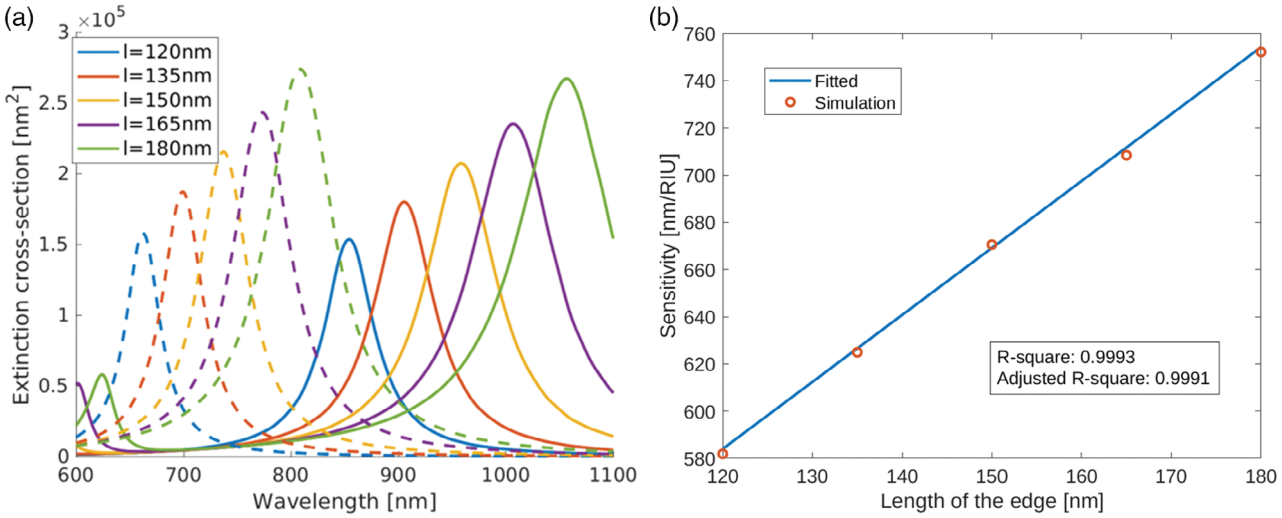

Figure 5. a) Position of the peak in air $n = 1.00$ (dashed line) and in water $n = 1.33$ (solid line) for multiple (l) side lengths ($t = 10$ nm, $\gamma = 0.1$) b) Bulk refractive index sensitivity as a function of the edge length (with a linear fit).

may not be entirely independent of each other, they were set independently in the simulation for systematic study.

The default edge length of 150 nm, thickness of 10 nm, and $\gamma = 0.1$ were used in all cases unless otherwise specified. The sensitivity was calculated from the simulated data in water ($n = 1.33$) and air ($n = 1.00$) media.

For the first two parameters, further examination was performed around the default values ($l = 150$ nm, $t = 10$ nm). Thereby, (−20%, −10%, 0%, 10%, 20%) were examined.

In addition to the sensitivities presented in the main text, the dependence of the extinction peak wavelength on geometric parameters (in water medium) is presented in the Supplementary Information, together with all data for the linear fits (Figures S3–S8, Supporting Information).

2.2.2. Edge Length

As the edge length increases, so does the location and intensity of the peak (**Figure 5**a). Thus, a standard deviation of particle size of $\Delta l = (15–20)\%$ can cause a deviation in peak position in simulations compared to experiments.

In this limited range, the sensitivity is directly proportional to size, with good accuracy (Figure 5b). The same is observed for the peak position.

2.2.3. Thickness

The position of the peak shifts toward smaller wavelengths as the thickness increases (**Figure 6**a). The standard deviation of the thickness has no significant effect on the intensity of the peak and has less of an effect on the position of the peak than the edge length. The effect of thickness variation may manifest in increasing the peak width. A similar proportion of thickness change has less effect than a change in edge length.

Higher thickness is associated with lower sensitivity; the linear fit again provides a good approximation of the investigated range. (Figure 6b).

2.2.4. γ (Roundness)

The largest possible cut-off radius is the radius of the circle inscribed in the triangle (the truncated triangle becomes a circle). The value of γ, in this case, can be derived from Heron's formula: $\gamma_{max} = \frac{1}{2\sqrt{3}} \approx 0.289$. The triangles, which are the bases of the prisms, were examined from the very pointed ($\gamma \approx 0$) to the very blunt $\gamma \approx 0.2$ (illustration in **Figure 7**).

The peak appears at longer wavelengths (**Figure 8**a), and the sensitivity is also higher for pointed particles than for rounded ones (Figure 8b). Despite the significant change in the shape between $\gamma = 0.03$ and $\gamma = 0.20$, the results are not as sensitive to this parameter as to the edge length.

Unlike the other two variables, the sensitivity and peak positions do not exhibit a clear linear dependence on γ. As roundness has little effect on sensitivity, its significance in the model is reduced. Therefore, assuming a linear relationship for the sake of simplification also has little effect on the final result. A unique feature of the γ parameter is that increasing it has an inverse effect on the primary and secondary peaks. For rounder particles, the two peaks are closer together in the spectrum.

2.2.5. Varying Multiple Parameters

The established relationship between sensitivity (and peak position) and geometric parameters is also true, even if several parameters change simultaneously. Only the constant $\gamma = 0.1$ case is included here (**Table 1**). However, the Supplementary Material section (Table S1, Supporting Information) contains the other raw data.

2.3. Surface Sensitivity

The results described so far assumed that the surface of the nanoparticle is not covered by a dielectric layer. However, in real scenarios, e.g., directly after synthesis or biofunctionalization,

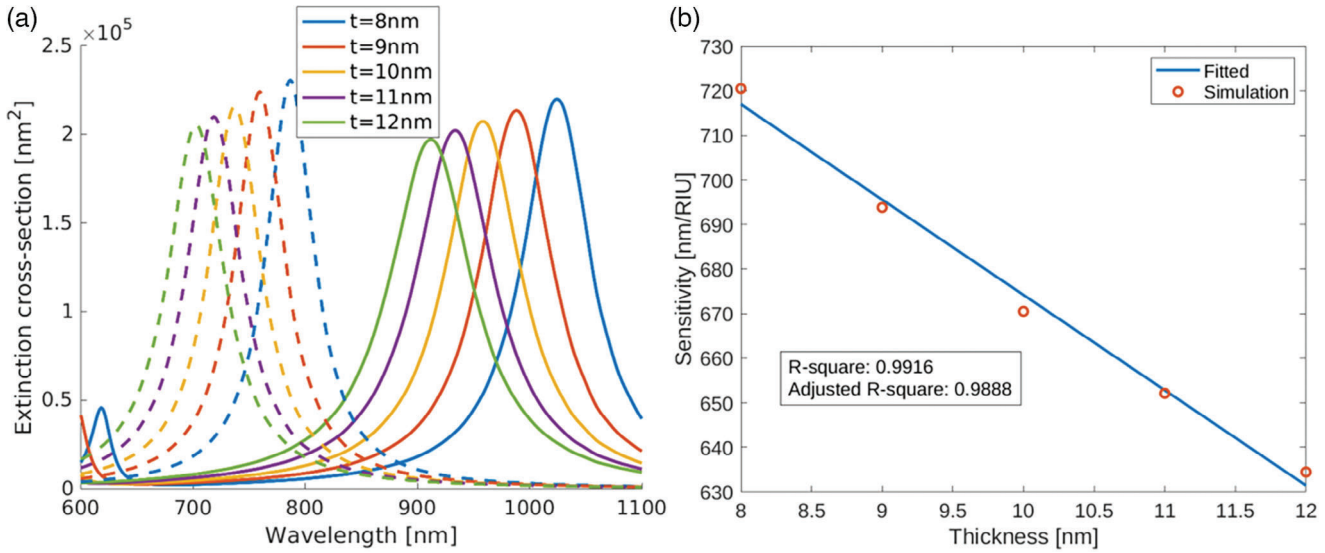

Figure 6. a) Position of the peak in air $n = 1.00$ (dashed line) and in water $n = 1.33$ (solid line) for multiple (t) thicknesses ($l = 150$ nm, $\gamma = 0.1$) b) Sensitivity as a function of thickness (with a linear fit).

the surface is covered with a thin molecular layer. To investigate the effect of this capping, a simulation of particles surrounded by a dielectric layer with a refractive index of 1.5 RIU was also performed. Even a thin layer can have a significant effect on both peak position (**Figure 9**a) and sensitivity (Figure 9b). The dielectric environment close to the particle, where the evanescent field is intensive, is more significant in sensing, as the evanescent field decays exponentially with increasing distance from the particle. So, the significance of that part of space filled with dielectric decreases similarly. Like a high refractive index bulk medium, a high refractive index capping causes the peak to shift toward longer wavelengths. Further thickening the capping causes less and less incremental change, and in the limit, it returns the bulk ($n = n_c$) value, where n_c is the refractive index of the capping.

The peak shift caused by capping also illustrates what happens to the sensitivity when the change in refractive index is localized near the particle (binding events). In this case, i.e., when the peak shift is caused by a dielectric layer on the surface (and not by a change in the refractive index of the bulk environment), the sensitivity is called surface sensitivity.

If the particle is capped, this has a negative effect on the bulk sensitivity. Just as a few 10 nm capping causes a significant peak shift, such a thin layer also significantly degrades the bulk sensitivity.

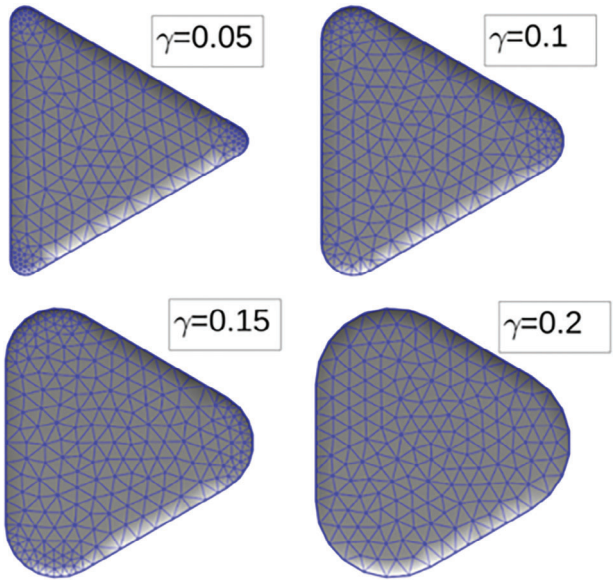

Figure 7. Nanoprisms from the top view at different γ (roundness) parameters.

2.4. Discussion and Experimental Relevance

The results of the simulations were compared with the data found in the literature (**Table 2**). In most cases, the reported sensitivity values are somewhat smaller than what would be estimated based on our numerical simulations (see **Figure 10** for a comparison), but there are some exceptions. The highest sensitivity was measured not on pure silver particles but on gold-coated edged composites.[35] It is also emphasized that the highest sensitivity was measured not on a single particle but on an ensemble of particles. Coupled plasmon resonance occurs on particles that are in close proximity to each other. This can increase the sensitivity compared to the single-particle case. The combination of coupled resonance and gold-coated edges resulted in a sensitivity of $S \approx 1800$ nm/RIU.

The work of Charles et al. investigates a set of geometric parameters (as presented in Figure 10). The sensitivity trend aligns well with our simulation results, although slightly lower values were measured, except for nanoparticles with the highest aspect ratios, where they measured exceptionally high sensitivities.[38] Their results were also supported by DDA simulation.

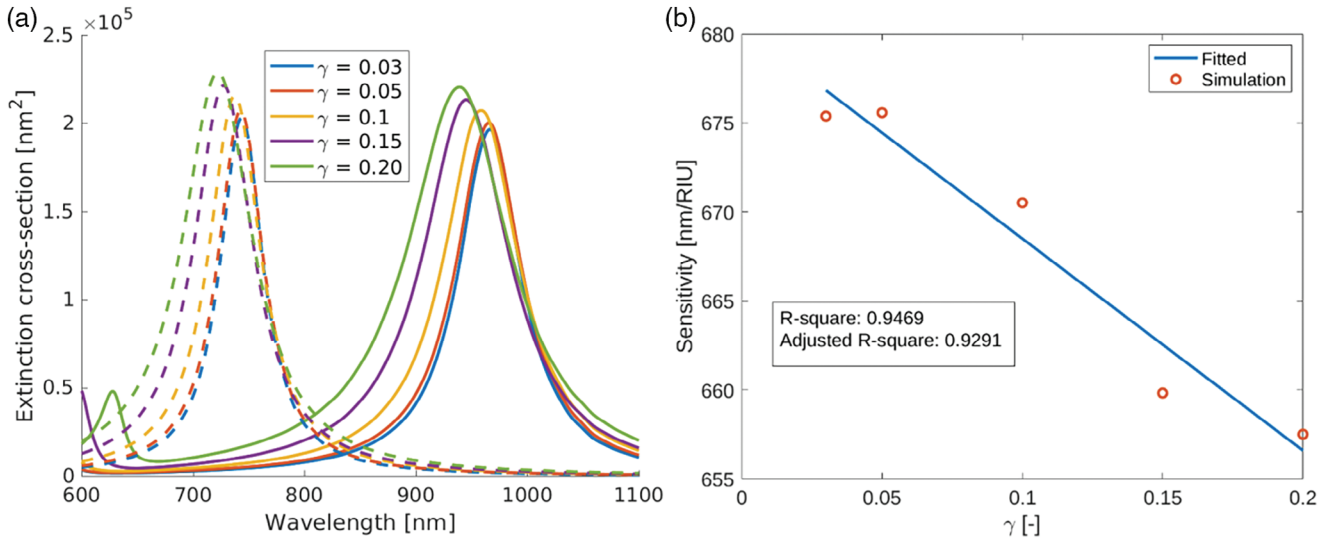

Figure 8. a) Position of the peak in air $n = 1.00$ (dashed line) and in aqueous medium $n = 1.33$ (solid line) for multiple γ values ($l = 150$ nm, $t = 10$ nm) b) Sensitivity as a function of γ (mismatched linear fit) for the simulations.

Interestingly, many articles use the NSL technique (nanosphere lithography) to fabricate triangular nanoparticles.[40–45] This approach uses a mask of densely packed polymer particles on a substrate for a subsequent metal deposition step. The removal of the sacrificial polymer particle monolayer results in triangular structures. Although these nanostructures resemble nanoprisms, they differ significantly from the chemically synthesized nanoparticles (e.g., different crystal structure, lack of molecular capping, attached to a solid support sometimes with metallic adhesion layers etc.). Thus, comparing them with colloidal particles or simulation results is not straightforward.

Figure 10 compares the simulation results with the available literature data. As shown, the simulation typically overestimates the sensitivity, but the deviation remains roughly constant, except for the experimental data of Charles et al. measured at the highest wavelengths. The main explanation for the systematic deviation can be the presence of dielectric capping. The capping can be induced by contamination or corrosion of the nanoparticles. As a result of corrosion, not only does a respective layer appear, but also the shape of the nanoparticles changes, which may also play a role in the systematic difference between the literature and simulation results.[56] The capping reduces the sensitivity and shifts the peak to a higher wavelength (Figure 9), while as a result of the size distribution – as will be presented below -, both the position of the peak and sensitivity increase, but the latter only to a lesser extent. Further differences may occur because of multiparticle interactions, irregularly shaped particles, or neglected quantum mechanical effects. However, discussion of these possibilities is beyond the scope of this manuscript.

Table 1. Refractive index sensitivity [nm/RIU] of the nanoprisms in the function of varied edge length and thickness at $\gamma = 0.1$.

	Thickness, t [nm]				
Length, l [nm]	8	9	10	11	12
120	630	603	582	566	550
135	675	650	625	606	590
150	720	694	671	652	635
165	758	736	708	687	674
180	803	773	752	731	711

2.5. Modeling Particle Distributions

As mentioned in Section 3.1, the most significant difference between the simulation and the experimental results is that only particles with discrete parameters can be investigated in the simulation, while the experimental samples contain a considerable number of particles that are not perfectly identical. A simple solution to the problem is presented in this chapter. For the sake of simplicity, the effect of a capping on the particle is neglected in this extended model. The extinction spectrum often exhibits a Lorentzian line shape.[57–60] Recognizing that this description accurately represents the single-particle spectra of the simulated prisms was crucial to creating a more realistic model. The main peak of the extinction spectrum (and also the other significant peaks) obtained as a result of the simulation can be approximated and fitted by a Lorentzian function, as in Equation (1):

$$\sigma_{ext}(\lambda) \approx \frac{p_1}{(\lambda - p_2)^2 + p_3} \tag{1}$$

The equation is written as a function of the wavelength in vacuum, like the other extinction spectra in this article, and not as a function of energy as is usual in spectroscopy.

The parameters corresponding to the properties of the vertex: $p_2 = q_1 = \lambda_0$ gives the location, $p_1 / p_3 = q_2 = \sigma_{max}$ gives the maximum extinction value and $\sqrt{p_3} = q_3 = \Gamma$ gives the half-width of the peak. Considering only the most significant k peaks, the

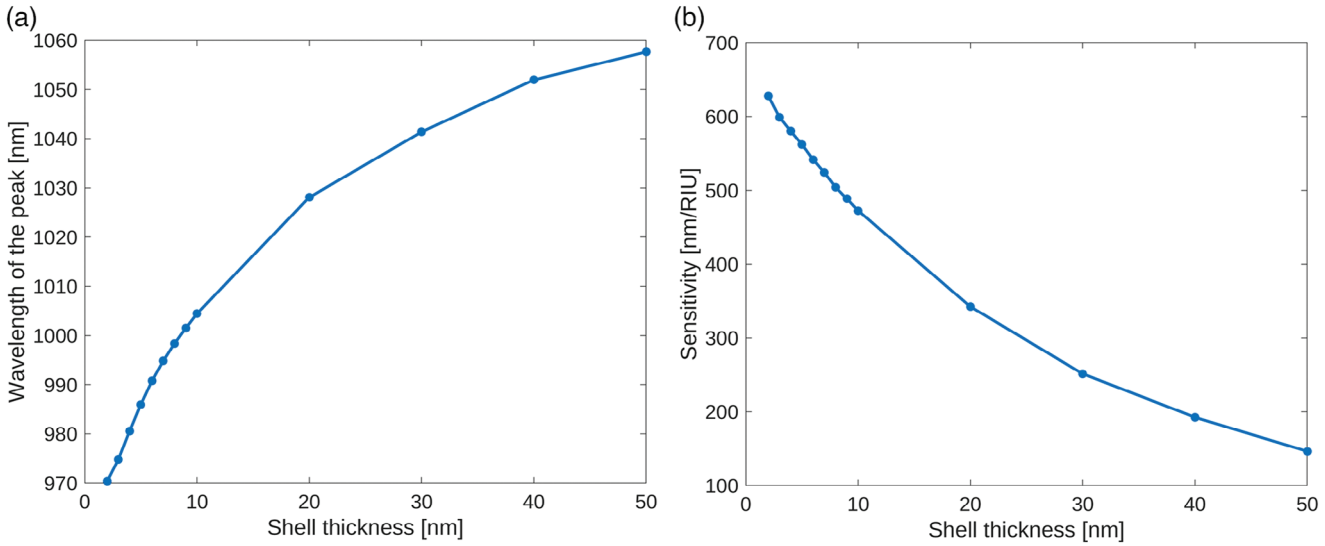

Figure 9. a) Position of the peak (calculated by simulation) as a function of dielectric shell ($n_c = 1.5$) thickness (the bulk dielectric environment is water ($n = 1.33$) b) The bulk refractive index sensitivity of a particle with the same dielectric capping.

Table 2. Performance of silver nanoprisms surveyed based on the literature.

Ref.	Edge length [nm]	Thickness [nm]	Peak (air) [nm]	Peak (water) [nm]	Sensitivity [nm/RIU]	Coating	Analyte/Medium
Xue[36]	88	24	–	≈630	413	–	glycerol
Shahjamali[37]	(>34)	–	–	687	402	- (and Au edge)	sucrose
Charles[38]	max. 197	14	–	1093	max. 1096	–	sucrose
Takahashi[39]	≈120	10	–	≈900	354±9	Ag@Au, (Ag@Au@TiO_2)	water, acetonitrile, hexane, chloroform
Haes[40]	100	30	–	561.4	191	SAM	streptavidin
Haes[41]	130.8	34.8	–	663.9	–	ADDL	ADDL
Haes[42]	90	25	–	–	≈200 (ref)	Anti-ADDL	ADDL
Hall[43]	100	80	–	≈674	≈241	SAM	Ca^{2+}
Ma[44]	115	42	626	–	–	-(and PMMA)	chloroform (vapor)
Brigo[45]	≈100	55	639	–	–	-(and Aryl-PSQ)	aromatic hydrocarbons
Xia[46]	70±10	7	–	755	–	–	glucose
Zhang[35]	max. 200	7±1	–	pure Ag: 1167, Au edge: 1185	max. 1816 (ensemble)	Au capping on the edge	C-reactive protein
Martinsson[47]	30-40	–	–	≈650	≈425	Au capping on the edge	bulk: sucrose, surface: bilayers of PAH/PSS and BSA adsorption
Ranjit[48]	50	–	636 (func)	≈752	–	SAM	Concanavalin A
Hedge[49]	35-50	–	–	≈800	sol.: 465, 461, immob: 193, 204	–	glucose and glycerol
Condorelli[50]	130 (and 40)	8-10	–	≈800	max. 269	–	sucrose
Scardaci[51]	70–80	10-20	–	≈500	>216	–	sucrose
Compagnini[52]	170±100	15±3	–	max. ≈1000	max. ≈450	–	sucrose
Potara[53]	115–123	11±2	–	618	387	chitosan	glycerol
Condorelli[54]	200	16	–	669	374	–	sucrose
Scardaci[55]	175	25	–	≈900	460	–	sucrose
Charles[38]	150	15	–	950–1100	≈700	–	sucrose

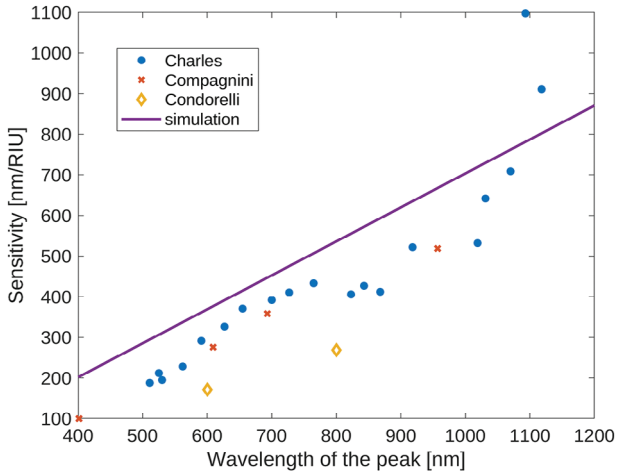

Figure 10. Sensitivity as a function of extinction peak wavelength (linear fit based on simulation and experimental data from literature sources: Charles,[38] Compagnini,[52] Condorelli[50]).

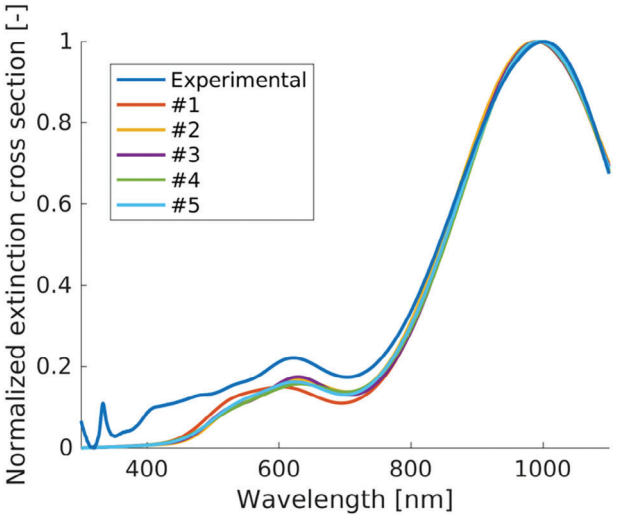

Figure 11. Comparison of experimental and modeled extinction spectra ($n = 1.33$). The five fitted curves correspond with the parameters presented in Table 3 (#1–#5).

spectrum can be approximated as in Equation (2).

$$\sigma_{ext\ mono}(l,t,\gamma) \approx \sum_{k=1}^{peak} \frac{q_{2k} \cdot q_{3k}^2}{(\lambda - q_{1k})^2 + q_{3k}^2} = \sum_{k=1}^{peak} \frac{\sigma_{max\ k}(l,t,\gamma) \cdot \Gamma_k^2(l,t,\gamma)}{(\lambda - \lambda_{0k}(l,t,\gamma))^2 + \Gamma_k^2(l,t,\gamma)} \quad (2)$$

The re-parameterization is advantageous because it can be assumed, to a good approximation, that these new parameters depend linearly on the variables (l, t, γ). (The linearity of these parameters is similar to the results presented in the description of the sensitivity of prisms (Figures 5, 6, and 8). In the case of (l, t), this approximation is still good, while for γ this assumption is used only for the sake of simplicity, which, however, does not cause a significant difference in terms of the final result.) Thus, a k peak can be characterized by position, height, and half-width parameters, which can be described in Equations (3) and (4).

$$q_{ik}(l,t,\gamma) = C_{ik0} + C_{ik1}l + C_{ik2}t + C_{ik3}\gamma = \sum_{m=0}^{3} C_{ikm}x_m \quad \text{where } i \in \{1,2,3\} \quad (3)$$

and

$$x_0 = 1, x_1 = l, x_2 = t, x_3 = \gamma \quad (4)$$

Using the fitted coefficients, the extinction spectrum of any particle within the linearity range can be generated.

For a particle in solution, it is assumed that the size distribution can be described by a Gaussian distribution. Thus, a multivariate Gaussian distribution was assumed, with expected values that correspond roughly to the parameters of the default particle. The standard deviations should be set to values corresponding to a real particle arrangement. The distribution was randomly sampled at 100 000 points. After summing and normalizing the sampled spectra, an extinction peak can be obtained, which already considers the fact that many different particles are present in a solution at the same time.

The model considered only the three main peaks with the highest intensities. To calculate sensitivity, the presented algorithm was also run for $n = 1$ refractive index in addition to $n = 1.33$ (aqueous medium).

To generate multivariate normal random numbers, and thus a spectrum of randomly parameterized prisms, three types of input data must be specified. In addition to the mean (μ_l, μ_t, μ_γ) and standard deviation (σ_l, σ_t, σ_γ) values belonging to the variables l, t and γ, the correlation coefficients R_{lt}, $R_{l\gamma}$, $R_{t\gamma}$ are also needed.

The new multivariate Gaussian distribution approach improves the agreement between simulated and experimentally measured extinction spectra compared to the previous single particle model. As before, for the single-particle case (Figure 3), the generated spectra were compared with the experimentally measured extinction cross-section. The results are shown in **Figure 11** and in **Table 3**.

As seen in the figure, with all the listed parameters, an almost equally good fit can be achieved. First (#1), it was investigated how much agreement could be obtained for the default particle case, leaving only the standard deviations as free parameters, and taking the correlation coefficients as 0. It was found that by tuning μ_l, μ_t between the realistic values, it is not possible to improve the fit. However, by tuning μ_γ (#2), the position of the secondary peak can also be obtained. (This is due to the fact that by adjusting γ, the positions of the main and secondary peaks can be shifted in different directions, as described in Section 3.2.4.) No significant improvement was obtained by tuning the correlation coefficients (#3, #5). The correlation coefficients could be inferred based on the kinetics of particle formation (which is beyond the scope of this article), but it was only assumed that these are positive numbers (and less than one). Unfortunately, due to the many free parameters, no information on their values can be obtained from the fittings. Fine-tuning μ_i parameters (#4) or free-tuning

Table 3. The parameters of the displayed modeling results, as presented in Figure 11.

No. fit	μ_l [nm]	μ_t [nm]	μ_γ [nm]	σ_l [nm]	σ_t [nm]	σ_γ [nm]	R_{lt}	$R_{l\gamma}$	$R_{t\gamma}$
#1	150	10	0.1	27.2	1.9	0.004	0	0	0
#2	150	10	0.15	32.9	0.3	0.007	0	0	0
#3	150	10	0.15	42.9	2.5	0.001	0.70	0.28	0.54
#4	151.9	9.5	0.14	22.5	2.4	0.006	0	0	0
#5	144.5	9.1	0.13	29.3	2.3	0.016	0.21	0.17	0.76

all parameters (#5), did not produce a significantly better fit than (#2). Therefore, this method cannot obtain exact data regarding the distribution of particles in the experimental sample. Due to the numerous free parameters, a similarly good agreement can be achieved even with very large, e.g., $\mu_l =$ 170 nm, or small, e.g. $\mu_l =$ 140 nm particles.

The limitations of the model are indicated by the fact that the secondary peak (the peak resulting from the merging of the two non-dominant considered peaks) is less intense than expected based on the experimental data.

For the shape and position of the dominant peak, which is the most important for sensing applications, a good fit is obtained with realistic values of the parameters characterizing the distribution of particles.

An important result is that in all the cases of particles with a wide variety of distributions, if the spectrum was consistent with the experimental results, the sensitivity was always very similar: $S = (695 \pm 5)$ nm/RIU. This is 25 nm/RIU higher than the result obtained by single-particle simulation.

The most important effects of considering particle distributions in the simulations are:

1) Broadening: The weighted sum of single-particle spectra has a larger full width at half maximum (FWHM) which approximates the experimental results better.
2) Redshift: It is observed for l and t parameters, that peaks with longer wavelengths are also more intense. (This is not true for γ, but it has less influence on the peak position than the other two parameters) Although for a Gaussian distribution the same amount (and same weight) of blueshifted as redshifted spectra contributed to the final result, the peaks of the latter are more intense, so the resulting peak is also redshifted compared to the peak of the default (average) particle.
3) Slight increase in sensitivity: As can be seen in Figure 10, redshift can be linked to an increase in sensitivity, so this is also to be expected. (Also note, that other results indicate that the increase is present only in the case of a sufficiently small standard deviation, and a decrease is expected in the case of a larger standard deviation. Furthermore, the slight increase in sensitivity does not compensate for the strong broadening of the extinction peak.)

All major discrepancies between simulated and experimental spectra arising in the single-particle simulation (such as the position and width of the main peak) can be explained and corrected by taking into account the distribution of the prism-shaped particles. This correction is possible even with the simplified model presented.

3. Conclusion

Silver nanoprisms were synthesized and examined using SEM. Based on the geometric parameters obtained from the SEM images, a model was constructed, and numerical simulations were performed to investigate the bulk refractive index sensitivity of these silver nanoprisms. The effect of their most important geometric parameters, namely the edge length (l), thickness: t, and roundness (γ) were studied. The mean parameters of the silver nanoprisms were: $l = 150$ nm, $t = 10$ nm and $\gamma = 0.1$. The deviations from these parameters were investigated in the range of ±20% for l and t, and between (0.03–0.2) for γ. The extinction peak wavelength of this default particle in water was 958 nm, while its sensitivity was 670 nm/RIU. Thinner nanoprisms with longer edges are preferred based on the simulations. However, it is important to consider the shift of the extinction peak into the near-infrared region for such nanoparticles. Sharper particles have a higher sensitivity, but this parameter was found to be less important than the other two. The approximately linear relationship between the sensitivity and these parameters is given over a wide range in the Table S1 (Supporting Information).

Literature data were also studied to compare the experimentally obtained sensitivities with the simulation results. Although the sensitivity values reported in the experiments were smaller than those predicted by the simulations, this deviation seemed to be systematic. The deviation in the results could be due to corrosion, sample contamination, or the substrate effect in certain experimental cases. Chapter 3.3 presented the effect of capping formation, which can cause differences between experimental and simulated sensitivity, and was illustrated with simulation results.

Given that geometric parameters are not discrete but can be approximated by Gaussian distributions, a novel extended simulation was performed. The first step was to fit the extinction peaks of individual prisms with Lorentzian functions. The subsequent objective was to investigate the dependence of the three parameters that define a Lorentzian function, namely peak position, intensity, and half-width, on l, t, and γ, respectively. A linear relationship was observed over the investigated range. By following these steps, it is possible to obtain the spectrum of an arbitrary prism quickly, without the need for further simulation. This method enables the inference of optical properties of systems with a size distribution by sampling a large number of individual cases. This method was used to calculate the extinction spectra and sensitivities of nanoprism systems. The calculations were performed for various mean values, standard deviations, and correlation coefficients, assuming a multivariate Gaussian distribution. The extended model resulted in a significantly improved match with the experimental extinction spectrum. It

accounts for the broadening and shifting of the extinction peak and predicts a slightly increased sensitivity of (695±5 nm/RIU). The presented model and data could be useful in designing and optimizing the geometric parameters of silver nanoprisms, which show a lot of promise for many emerging application areas connected to plasmonics.

4. Experimental Section

Chemicals and Materials: All chemicals were used as received from the following suppliers. Silver nitrate (Rotimetic 6N, 99.9999%, Roth KG, Karlsruhe, Germany), sodium borohydride (fine granular for synthesis, Merck KGaA, Darmstadt, Germany), poly(sodium styrenesulphonate) (PSSS, average $M_w \approx 1\,000\,000$, Sigma-Aldrich, Taufkirchen, Germany), and sodium citrate dihydrate (pro analysis, Merck) were used for the synthesis of the Ag seed nanoparticles. For the growth step, ascorbic acid (99+%, Alfa Aesar, Karlsruhe, Germany) was used as a reducing agent.

Synthesis Parameters: Silver nanoprisms were synthesized using a two-step method based on Aherne et al.[61] with minor modifications. The process of synthesis is illustrated in the Figure S1 (Supporting Information). Silver seed nanoparticles were synthesized following the original procedure. Briefly, 4.865 ml water, 0.5 ml of 25 mM trisodium citrate, 125 µl of 1 g/l PSSS, and 60 µl of 50 mM freshly prepared sodium borohydride were mixed in a well-agitated 20 ml glass vial. 5 ml of 0.5 mM silver nitrate solution was added with a syringe pump at a flow rate of 2 ml min^{-1}. The final particles were synthesized by mixing 4.97 ml water and 21 µl of 40 mM ascorbic acid in a well-agitated 20 ml glass vial. Ten microliter of the as-prepared seed solution was added, and after 15 s, a solution of 3 ml 0.5 mM silver was added at a flow rate of 1 ml min^{-1}. Thirty seconds after the addition was finished, 0.5 ml of 25 mM trisodium citrate was added to stabilize the particles.

The resulting particles were characterized using scanning electron microscopy (SEM, S-4800, Hitachi Europe, Düsseldorf, Germany) and UV–vis spectroscopy (Specord 200, Analytik Jena, Jena, Germany). For the SEM measurements, the particles were centrifuged and dropped onto a silicon chip. After drying the particles in air, the chip was washed multiple times with water before the measurements.

BEM Simulation Details: The simulations were performed using the MNPBEM toolbox, which is an implementation of the boundary element method (BEM) in MATLAB specifically designed for plasmonics applications.[28] The simulated particles were thin triangular plates with rounded corners. An essential input parameter for the simulations is the wavelength-dependent refractive index table of the nanoparticle material. The dielectric function of silver was taken from McPeak's results.[62] Plane wave excitation was applied as excitation, and the retarded solver (solving Maxwell's full equations) was selected for more accurate results. The result of a single simulation is the extinction cross-section of the given particle. Depending on the refractive index of the medium surrounding the nanoparticle, the extinction peak shifts. The shift can be used to calculate the bulk refractive index sensitivity, which is the most common benchmark of nanoparticle sensors.[63] Bulk refractive index sensitivity is defined as the wavelength shift of the extinction peak per unit change in the refractive index of the surrounding bulk medium.[64] Media with refractive indices of $n = 1.00$ (air) and $n = 1.33$ (water) were used to calculate this sensitivity.

Since the simulations were carried out, the more advanced NANOBEM toolbox has superseded the MNPBEM toolbox.[65] The descendant is also a BEM approach, but it is based on the Galerkin scheme[32,66,67] instead of the collocation approach for the electrodynamic potentials used by MNPBEM.[68]

Supporting Information

Supporting Information is available from the Wiley Online Library or from the author.

Acknowledgements

The authors acknowledge KIFÜ for awarding access to computational resources based in Hungary at Debrecen. This research was supported by the EU-funded Hungarian grant EFOP-3.6.2-16-2017-00005. The research reported in this paper and partially carried out at the Budapest University of Technology and Economics has been supported by the National Research, Development, and Innovation Fund of Hungary under Grant TKP2021-EGA-02. The research was also supported by the National Research and Innovation Office under project number 2020–1.2.3-EUREKA-2022-00030 and by the Nanoplasmonic Laser Fusion Research Laboratory project (2022-2.1.1-NL-2022-00002). The work at TU Ilmenau was funded by the Deutsche Forschungsgemeinschaft DFG with the grant KO1403/45-1 which is gratefully acknowledged. The SEM images were acquired at the IMN MacroNano ZMN facility. The work at the Leibniz-IPHT as a part of Leibniz Health Technologies was supported by DFG (FR 1348/31-1), by EUREKA/BMBF (HeavySense, 01DS23017B) and by DAAD (ID 57561797). A.B. and G.S. are grateful to the Deutscher Akademischer Austausch Dienst (DAAD) and Tempus Foundation (TKA) for supporting the "Development of plasmonic hybrid optical biosensors" (TKA- 160590) bilateral project. A.B. is also grateful for the support of the Hungarian Academy of Engineering and the "MICHELBERGER MESTERDÍJ" Scholarship.

Conflict of Interest

The authors declare no conflict of interest.

Data Availability Statement

The data that support the findings of this study are available in the supplementary material of this article.

Keywords

boundary element method, bulk refractive index sensitivity, localized surface plasmon resonance, particle distribution, silver nanoprisms

Received: November 21, 2023
Revised: January 15, 2024
Published online:

[1] K. M. Mayer, J. H. Hafner, *Chem. Rev.* **2011**, *111*, 3828.
[2] S. Sadanandan, V. S. Meenakshi, K. Ramkumar, N. P. Pillai, P. Anuvinda, P. J. Sreelekshmi, V. Devika, K. Ramanunni, R. Jeevan Sankar, M. M. Sreejaya, *Food Control* **2023**, *148*, 109510.
[3] K. E. Fong, L.-Y. L. Yung, *Nanoscale* **2013**, *5*, 12043.
[4] J. W. Ha, *Appl. Spectrosc. Rev.* **2022**, *58*, 346.
[5] M.-C. Daniel, D. Astruc, *Chem. Rev.* **2003**, *104*, 293.
[6] L. Li, W. Cui, Z. He, W. Xue, H. He, *Plasmonics* **2022**, *17*, 1231.
[7] J. Yguerabide, E. E. Yguerabide, *Anal. Biochem.* **1998**, *262*, 137.
[8] J. Yguerabide, E. E. Yguerabide, *Anal. Biochem.* **1998**, *262*, 157.
[9] B. J. Wiley, S. H. Im, Z.-Y. Li, J. McLellan, A. Siekkinen, Y. Xia, *J. Phys. Chem. B* **2006**, *110*, 15666.
[10] C. Sönnichsen, A. P. Alivisatos, *Nano Lett.* **2004**, *5*, 301.
[11] A. Knauer, J. M. Koehler, *Phys. Chem. Chem. Phys.* **2016**, *18*, 15943.
[12] J. Pérez-Juste, I. Pastoriza-Santos, L. Liz-Marzán, P. Mulvaney, *Coord. Chem. Rev.* **2005**, *249*, 1870.
[13] V. Pellas, F. Sallem, J. Blanchard, A. Miche, S. M. Concheso, C. Méthivier, M. Salmain, S. Boujday, *Talanta* **2023**, *255*, 124245.
[14] P. Szustakiewicz, G. González-Rubio, L. Scarabelli, W. Lewandowski, *ChemistryOpen* **2019**, *8*, 705.

[15] E. Podlesnaia, P. Gerald Inangha, J. Vesenka, M. Seyring, H.-J. Hempel, M. Rettenmayr, A. Csáki, W. Fritzsche, *Small* **2023**, *19*, 2204810.
[16] S. Barbosa, A. Agrawal, L. Rodríguez-Lorenzo, I. Pastoriza-Santos, R. A. Alvarez-Puebla, A. Kornowski, H. Weller, L. M. Liz-Marzán, *Langmuir* **2010**, *26*, 14943.
[17] H.-L. Wu, C.-H. Kuo, M. H. Huang, *Langmuir* **2010**, *26*, 12307.
[18] J.-E. Park, Y. Lee, J.-M. Nam, *Nano Lett.* **2018**, *18*, 6475.
[19] J. Pan, W. Wang, M. Ji, X. Xing, Z. Lu, *Cryst. Growth Des.* **2023**, *23*, 2203.
[20] X. Xu, M. Cortie, *Adv. Funct. Mater.* **2006**, *16*, 2170.
[21] S. E. Skrabalak, J. Chen, Y. Sun, X. Lu, L. Au, C. M. Cobley, Y. Xia, *Acc. Chem. Res.* **2008**, *41*, 1587.
[22] G. González-Rubio, L. Scarabelli, A. Guerrero-Martınez, L. M. Liz-Marzán, *ChemNanoMat* **2020**, *6*, 698.
[23] S. Farooq, F. Wali, D. M. Zezell, R. E. de Araujo, D. Rativa, *Polymers* **2022**, *14*, 1592.
[24] H. Chatterjee, D. Bardhan, S. K. Pal, K. Yanase, S. K. Ghosh, *J. Phys. Chem. Lett.* **2021**, *12*, 4697.
[25] A. Yakoubi, C. E. B. Dhafer, *Plasmonics* **2022**, *18*, 311.
[26] P. Mandal, B. Tewari, *Surf. Interfaces* **2022**, *28*, 101655.
[27] D. Semeniak, D. F. Cruz, A. Chilkoti, M. H. Mikkelsen, *Adv. Mater.* **2022**, *35*, 2107986.
[28] U. Hohenester, A. Trügler, *Comput. Phys. Commun.* **2012**, *183*, 370.
[29] A. Amirjani, S. K. Sadrnezhaad, *J. Mater. Chem. C* **2021**, *9*, 9791.
[30] V. Myroshnychenko, J. Rodríguez-Fernández, I. Pastoriza-Santos, A. M. Funston, C. Novo, P. Mulvaney, L. M. Liz-Marzán, F. J. García de Abajo, *Chem. Soc. Rev.* **2008**, *37*, 1792.
[31] L. Cheng, G. Zhu, G. Liu, L. Zhu, *Mater. Res. Express* **2020**, *7*, 125009.
[32] U. Hohenester, *Nano and Quantum Optics*, Springer International Publishing, New York **2020**.
[33] L. B. Kiss, J. Söderlund, G. A. Niklasson, C. G. Granqvist, *Nanotechnology* **1999**, *10*, 25.
[34] C. G. Granqvist, R. A. Buhrman, J. Wyns, A. J. Sievers, *Phys. Rev. Lett.* **1976**, *37*, 625.
[35] Y.i Zhang, D. E. Charles, D. M. Ledwith, D. Aherne, S. Cunningham, M. Voisin, W. J. Blau, Y. K. Gun'ko, J. M. Kelly, M. E. Brennan-Fournet, *RSC Adv.* **2014**, *4*, 29022.
[36] B. Xue, D. Wang, J. Zuo, X. Kong, Y. Zhang, X. Liu, L. Tu, Y. Chang, C. Li, F. Wu, Q. Zeng, H. Zhao, H. Zhao, H. Zhang, *Nanoscale* **2015**, *7*, 8048.
[37] M. M. Shahjamali, M. Salvador, M. Bosman, D. S. Ginger, C. Xue, *J. Phys. Chem. C* **2014**, *118*, 12459.
[38] D. E. Charles, D. Aherne, M. Gara, D. M. Ledwith, Y. K. Gun'ko, J. M. Kelly, W. J. Blau, M. E. Brennan-Fournet, *ACS Nano* **2009**, *4*, 55.
[39] Y. Takahashi, K. Suga, T. Ishida, S. Yamada, *Anal. Sci.* **2016**, *32*, 275.
[40] A. J. Haes, R. P. V. Duyne, *J. Am. Chem. Soc.* **2002**, *124*, 10596.
[41] A. J. Haes, W. P. Hall, L. Chang, W. L. Klein, R. P. V. Duyne, *Nano Lett.* **2004**, *4*, 1029.
[42] A. J. Haes, L. Chang, W. L. Klein, R. P. V. Duyne, *J. Am. Chem. Soc.* **2005**, *127*, 2264.
[43] W. P. Hall, J. Modica, J. Anker, Y. Lin, M. Mrksich, R. P. V. Duyne, *Nano Lett.* **2011**, *11*, 1098.
[44] W. Ma, J. Luo, W. Ling, W. Wang, *Micro Nano Lett.* **2013**, *8*, 111.
[45] L. Brigo, N. Michieli, L. Artiglia, C. Scian, G. A. Rizzi, G. Granozzi, G. Mattei, A. Martucci, G. Brusatin, *ACS Appl. Mater. Interfaces* **2014**, *6*, 7773.
[46] Y. Xia, J. Ye, K. Tan, J. Wang, G. Yang, *Anal. Chem.* **2013**, *85*, 6241.
[47] E. Martinsson, M. M. Shahjamali, K. Enander, F. Boey, C. Xue, D. Aili, B. Liedberg, *J. Phys. Chem. C* **2013**, *117*, 23148.
[48] C. R. Yonzon, E. Jeoung, S. Zou, G. C. Schatz, M. Mrksich, R. P. V. Duyne, *J. Am. Chem. Soc.* **2004**, *126*, 12669.
[49] H. R. Hegde, S. Chidangil, R. K. Sinha, *Sens. Actuators A: Phys.* **2020**, *305*, 111948.
[50] M. Condorelli, L. Litti, M. Pulvirenti, V. Scardaci, M. Meneghetti, G. Compagnini, *Appl. Surf. Sci.* **2021**, *566*, 150701.
[51] V. Scardaci, M. Condorelli, M. Barcellona, L. Salemi, M. Pulvirenti, M. E. Fragalà, G. Compagnini, *Appl. Sci.* **2021**, *11*, 8949.
[52] G. Compagnini, M. Condorelli, M. E. Fragalà, V. Scardaci, I. Tinnirello, O. Puglisi, F. Neri, E. Fazio, *J. Nanomater.* **2019**, *2019*, 7084731.
[53] M. Potara, A.-M. Gabudean, S. Astilean, *J. Mater. Chem.* **2011**, *21*, 3625.
[54] M. Condorelli, V. Scardaci, L. D'Urso, O. Puglisi, E. Fazio, G. Compagnini, *Appl. Surf. Sci.* **2019**, *475*, 633.
[55] V. Scardaci, M. Pulvirenti, M. Condorelli, G. Compagnini, *J. Mater. Chem. C* **2020**, *8*, 9734.
[56] V. J. Keast, T. A. Myles, N. Shahcheraghi, M. B. Cortie, *J. Nanoparticle Res.* **2016**, *18*, 45.
[57] F. M. Balci, S. Sarisozen, N. Polat, C. M. Guvenc, U. Karadeniz, A. Tertemiz, S. Balci, *Nanoscale Adv.* **2021**, *3*, 1674.
[58] W. A. Jacak, *J. Phys. Chem. C* **2015**, *119*, 6749.
[59] C.-p. Huang, X.-g. Yin, H. Huang, Y.-y. Zhu, *Opt. Express* **2009**, *17*, 6407.
[60] N. Verellen, F. López-Tejeira, R. Paniagua-Domínguez, D. Vercruysse, D. Denkova, L. Lagae, P. Van Dorpe, V. V. Moshchalkov, J. A. Sánchez-Gil, *Nano Lett.* **2014**, *14*, 2322.
[61] D. Aherne, D. M. Ledwith, M. Gara, J. M. Kelly, *Adv. Funct. Mater.* **2008**, *18*, 2005.
[62] K. M. McPeak, S. V. Jayanti, S. J. P. Kress, S. Meyer, S. Iotti, A. Rossinelli, D. J. Norris, *ACS Photonics* **2015**, *2*, 326.
[63] M. D. Malinsky, K. L. Kelly, G. C. Schatz, R. P. V. Duyne, *J. Phys. Chem. B* **2001**, *105*, 2343.
[64] M. M. Miller, A. A. Lazarides, *J. Phys. Chem. B* **2005**, *109*, 21556.
[65] U. Hohenester, N. Reichelt, G. Unger, *Comput. Phys. Commun.* **2022**, *276*, 108337.
[66] W. C. Chew, *Waves and Fields in Inhomogenous Media*, IEEE, **1999**, http://dx.doi.org/10.1109/9780470547052.
[67] A. M. Kern, O. J. F. Martin, *J. Opt. Soc. Am. A* **2009**, *26*, 732.
[68] F. J. G. de Abajo, A. Howie, *Phys. Rev. B* **2002**, *65*, 115418.